

Assessing model-based carbon and oxygen abundance derivation from ultraviolet emission lines in AGNs

E. Pérez-Montero,¹★ R. Amorín^{2,3}, B. Pérez-Díaz^{2,1}, J. M. Vílchez¹ and R. García-Benito¹

¹*Instituto de Astrofísica de Andalucía, CSIC, Apartado de correos 3004, 18080 Granada, Spain*

²*Instituto de Investigación Multidisciplinar en Ciencia y Tecnología, Universidad de La Serena, Raul Bitrán 1305, La Serena, Chile*

³*Departamento de Astronomía, Universidad de La Serena, Av. Juan Cisternas 1200 Norte, La Serena, Chile*

Accepted 2023 February 23. Received 2023 February 23; in original form 2022 October 24

ABSTRACT

We present an adapted version of the code HII-CHI-MISTRY-UV to derive chemical abundances from emission lines in the ultraviolet, for use in narrow line regions (NLR) of active galactic nuclei (AGN). We evaluate different ultraviolet emission line ratios and how different assumptions about the models, including the presence of dust grains, the shape of the incident spectral energy distribution, or the thickness of the gas envelope around the central source, may affect the final estimates as a function of the set of emission lines used. We compare our results with other published recipes for deriving abundances using the same emission lines and show that deriving the carbon-to-oxygen abundance ratio using C III] λ 1909 Å and O III] λ 1665 Å emission lines is a robust indicator of the metal content in AGN that is nearly independent of the model assumptions, similar to the case of star-forming regions. Moreover, we show that a prior determination of C/O allows for a much more precise determination of the total oxygen abundance using carbon UV lines, as opposed to assuming an arbitrary relationship between O/H and C/O, which can lead to non-negligible discrepancies.

Key words: galaxies: active – galaxies: abundances – galaxies: evolution – galaxies: ISM – galaxies: nuclei – galaxies: Seyfert.

1 INTRODUCTION

Active Galactic Nuclei (AGN) host one of the most powerful energy sources in the Universe. The intense radiation field emanating from the hot accretion discs around supermassive black holes in galactic centres produces very bright emission lines from the surrounding gas. From this, various physical properties and chemical abundances in these regions can later be inferred up to a very high redshift, which can serve as indicators of the evolution of the universe at different cosmic epochs.

The UV region is of outstanding importance in this context. Several bright emission lines produced by AGNs, such as N V, He II, C IV, O III], and C III], which are sensitive to the ionization conditions and physical properties (i.e. electron density and temperature) of the warm ISM (e.g. Kewley, Nicholls & Sutherland 2019), can be identified in the $\lambda \sim 1000\text{--}2000$ Å region. While this range at $z \lesssim 2$ is typically explored using the *Hubble Space Telescope* (HST; e.g. Rigby et al. 2018; Berg et al. 2022), these lines are redshifted to rest-optical wavelengths at $z \sim 2\text{--}4$. Therefore, deep optical spectroscopic surveys with ground-based telescopes of 8–10 m class (e.g. Steidel et al. 2003; Shapley et al. 2003; Lilly et al. 2007a; Kurk et al. 2013; Le Fèvre et al. 2015; McLure et al. 2018) are typically efficient at detecting the largest samples of UV line emitters (e.g. Steidel et al. 2014; Maseda et al. 2017; Amorín et al. 2017; Nakajima et al. 2018a; Le Fèvre et al. 2019; Feltre et al. 2020; Saxena et al. 2020, 2022; Schmidt et al. 2021; Llerena et al. 2022).

Classical methods for determining chemical abundance are instead mostly based on rest-optical emission lines (e.g. Maiolino & Mannucci 2019). However, for galaxies at $z \sim 2\text{--}3$, these are redshifted to the near-infrared (NIR) and detections are often limited to the few bright lines (e.g. Steidel et al. 2014; Shapley et al. 2015). Joint analysis of the observed rest-UV and rest-optical emission spectra with predictions from detailed photoionization models for both star-forming galaxies (e.g. Gutkin, Charlot & Bruzual 2016; Pérez-Montero & Amorín 2017; Byler et al. 2018) and AGNs (e.g. Feltre, Charlot & Gutkin 2016b; Nakajima et al. 2018b; Dors et al. 2019; Hirschmann et al. 2019; Mignoli et al. 2019) thus emerge as powerful diagnostics for the ionization and chemical abundances of galaxies (e.g. Patricio et al. 2016; Vanzella et al. 2016; Amorín et al. 2017; Byler et al. 2020) and pave the way for similar analyses at higher redshifts with the JWST (e.g. Chevallard et al. 2019; Rigby et al. 2021).

The derivation of the metal content in the Narrow Line Region (NLR) of AGN galaxies from optical collisionally excited lines (CELs) is much more complex than in the case of star-forming regions, since the direct method (i.e. based on the prior determination of the electron temperature) can significantly underestimate the derived oxygen abundances (e.g. Dors et al. 2015), which are often considered as proxies for gas metallicity in galaxies. Instead, there are several studies dealing with the determination of different elemental abundances in AGN based on pure photoionization models (e.g. Storchi-Bergmann et al. 1998; Castro et al. 2017; Thomas et al. 2019) or on models assuming shocks in combination with photoionization (e.g. Dors et al. 2021).

* E-mail: epm@iaa.es

In the case of UV emission lines, since direct determination of chemical abundances in AGN is still not reliable, many of the various approaches pursued are also based on photoionization models, including detailed models for individual objects (e.g. Davidson 1977; Osmer 1980; Gaskell, Shields & Wampler 1981; Uomoto 1984; Hamann & Ferland 1992; Ferland et al. 1996; Dietrich & Wilhelm-Erkens 2000; Hamann et al. 2002; Shin et al. 2013; Feltre, Charlot & Gutkin 2016a; Yang et al. 2017). For a large number of objects, other authors propose calibrations of some UV emission line ratios sensitive to chemical abundance in these detailed models (e.g. Dors et al. 2014, 2019), or compare them in model-based diagnostic diagrams (e.g. Nagao, Maiolino & Marconi 2006; Matsuoka et al. 2009, 2018).

Another strategy suitable for use in large surveys is to use a Bayesian-like comparison between the adequate emission line ratios and the predictions from large model grids (e.g. Mignoli et al. 2019). This method has the advantage of better quantifying uncertainties and easily specifying the assumptions required when the number of emission lines input is limited. For example, the use of photoionization models, which include various combinations of C/O and O/H has great significance for estimating gas-phase metallicity in cases where very few C lines (e.g. C IV λ 1549 Å and C III λ 1909 Å) UV emission lines can be measured.

In this work, we present an adapted version of the code HII-CHI-MISTRY-UV (hereafter, HCM-UV, Pérez-Montero & Amorín 2017), originally developed for deriving O/H and C/O from UV emission lines in star-forming regions, for application to the NLR of AGN. The code is based on HCM (Pérez-Montero 2014), which deals with optical emission lines for deriving O/H and N/O ratios in star-forming regions, and has been extended for use in the NLR of AGN in Pérez-Montero et al. (2019).

The above work has shown that when applied to star-forming galaxies, the abundances provided by the HCM version using optical emission lines are in complete agreement with those provided by the direct method, while for AGNs they are in agreement with the expected metallicities at the centres of their host galaxies (Dors et al. 2020). This new version of the HCM-UV code is potentially useful for constraining the metallicity of the NLR of AGN up to very high redshift, and also provides a solution to the constraint imposed by using carbon emission lines to derive oxygen abundances, since it also estimates C/O.

The paper is organized as follows: In Section 2, we describe the method for deriving chemical oxygen and carbon abundances in the NLR of AGN from their UV emission lines, based on the code HCM-UV. In the same section, we describe our grids of photoionization models and we discuss their validity under different assumptions and for using different sets of emission lines. In Section 3, we apply the method to a sample of compiled data on UV lines for NLR in AGNs, and in Section 4, we discuss the results and compare them with other published calibrations based on the same available emission lines. Finally, in Section 5, we summarize our results and draw our conclusions.

2 DESCRIPTION OF THE METHOD

The method discussed in this paper is the adaptation of the code HCM-UV, originally developed for use with star-forming objects (Pérez-Montero & Amorín 2017), to the NLR of AGN. The extension of different versions of the code for use on AGN has already been done for optical lines by Pérez-Montero et al. (2019) and for infrared lines by Pérez-Díaz et al. (2022). In this section, we discuss the model grids that the code uses to estimate O/H, C/O, and the ionization

parameter ($\log U$) in these objects, as well as the defined observables based on the most typical UV emission line flux ratios that the code uses to derive these properties using a Bayesian-like methodology. Finally, we discuss how different assumptions for the models and the emission lines used affect the results.

The version of the code described here (v. 5.0) along with other versions prepared for use in other spectral domains, is publicly available.¹

2.1 Description of the models

The entire grid of models used in HCM-UV was calculated using the photoionization code CLOUDY v.17.01 (Ferland et al. 2017), which assumes a point-like central ionization source surrounded by a gas distribution. The models partially correspond to those of the optical version of the code described in Pérez-Montero et al. (2019), taking into account a spectral energy distribution (SED) with two components: one for the Big Blue bump peaking at 1 Ryd, and the other represented by a power law with spectral index $\alpha_x = -1$ for the non-thermal X-rays. For the continuum between 2 keV and 2500 Å, we considered a power law with two possible values for the spectral index $\alpha_{ox} = -0.8$ and -1.2 . The first value fits better the emission line fluxes in tailored models by Dors et al. (2017), while the second value fits better the average value found by Miller et al. (2011) in a sample of Seyfert-2 galaxies. For the gas, we assumed a filling factor of 0.1 and a constant density of 500 cm^{-3} , as is typical in the NLRs around type 2 AGNs (Dors et al. 2014). As discussed in Pérez-Montero et al. (2019) for the optical version of the code, assuming a higher value by $2 \times 10^3 \text{ cm}^{-3}$ does not lead to large deviations in the obtained results. Different grids were calculated considering the criterion of stopping the models and measuring the resulting spectrum as a function of the fraction of free electrons (f_e) in the last zone (i.e. the outermost with respect to the ionizing source). In some grids, we considered a fraction of 98 per cent and in others a fraction of 2 per cent. All chemical abundances were scaled to oxygen according to the solar proportions given by Asplund et al. (2009), except for nitrogen and carbon, which are in solar proportion, but whose relation to oxygen was left in the models as an additional free input parameter. Finally, we considered models with a dust-to-gas ratio that assumes the default value of the Milky Way, and also other models that do not consider the existence of dust mixed with the gas. Although a larger variety in the assumptions of dust composition and proportions would be more realistic, since these cannot be constrained from the input emission-line fluxes, these have not been more deeply explored in our grid of models, avoiding an unnecessarily high number of models in our grids.

Overall, the models in each grid cover the range of $12 + \log(\text{O/H})$ from 6.9 to 9.1 in bins of 0.1 dex, and values of $\log(\text{C/O})$ from -1.4 to 0.6 in bins of 0.125 dex. In addition, all models consider values of $\log U$ from -4.0 to -0.5 in bins of 0.25 dex. This gives a total number of 5865 models for each of the resulting grids. Considering additionally the two possible values of α_{ox} (-0.8 and -1.2), the two possible values of f_e in the outermost zone (2 or 98 per cent) and the existence or absence of dust grains mixed with the gas, we obtain a number of 8 different calculated grids.

¹In the webpage <http://www.iaa.csic.es/~epm/HII-CHI-mistry.html>

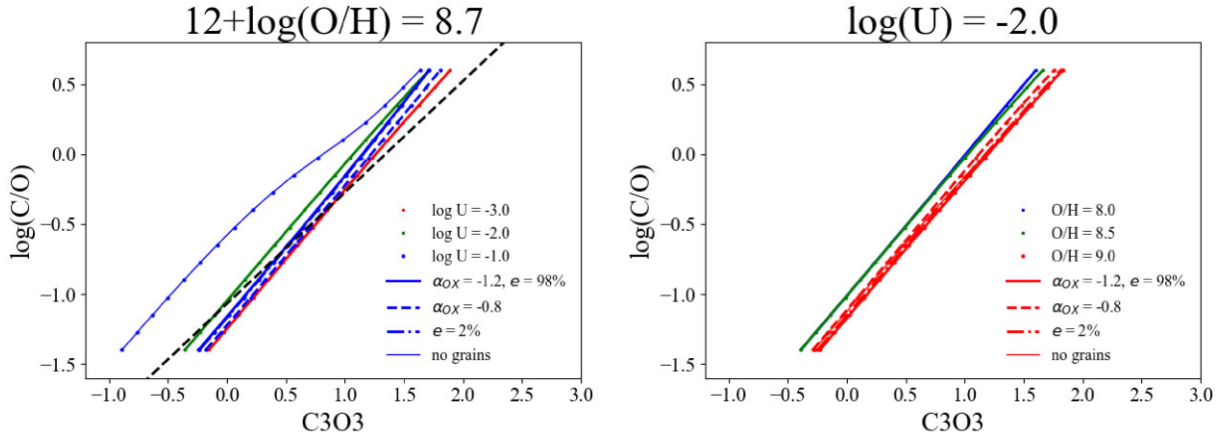


Figure 1. Relationship between emission line ratio C3O3 and $\log(C/O)$ for model sequences with different values of input parameters (left for fixed $12 + \log(O/H) = 8.7$, and right for fixed $\log(U) = -2.0$). The solid lines represent models for $\alpha_{OX} = -1.2$, f_e in the outermost zone of 98 per cent and considering dust grains. The other lines change only one parameter with respect to this sequence. The dashed line represents models with $\alpha_{OX} = -0.8$, the dot-dashed line represents models with f_e of 2 per cent, and the thin line represents models without grains. In the left-hand panel, the black dashed line represents the linear fit for models of star-forming galaxies that are in Pérez-Montero & Amorín (2017).

2.2 The HCM-UV code adapted for AGNs

The version of the code we describe here for its use for NLRs in AGNs follows a procedure similar to that used in other versions for other spectral regions, such as the optical (Pérez-Montero 2014) or the IR (Fernández-Ontiveros et al. 2021). In all cases, the code performs a Bayesian-like calculation that compares certain emission line fluxes and their errors with the results of the models in each grid. Here, we discuss the results obtained with the model grids described above. However, this new version of the code allows the user to use alternative grids as input models that have the same format as the default models.

The above comparison performed by HCM-UV to calculate the corresponding final mean values uses as weights for each model the χ^2 values of some defined specific emission line ratios that are sensitive to the properties we want to derive, as described in Pérez-Montero (2014). The uncertainties of the derived abundances and U are calculated as the quadratic addition of the weighted standard deviation and the dispersion of the results after a Monte Carlo simulation, using the input errors as random perturbations around the nominal introduced values for each emission flux.

The list of UV emission lines allowed as input by HCM-UV, for both SF and AGN, includes: Ly α at λ 1216 Å, C IV λ 1549 Å, O III] λ 1665 Å, and C III] λ 1909 Å. In addition, the code provides the ability to input optical emission lines H β and [O III] λ 5007 Å to obtain estimates of abundances using emission line ratios that are sensitive to electron temperature, as is the case with 5007/1665 (Pérez-Montero & Amorín 2017).

Unlike the previous version for star-forming galaxies, this version also includes the emission lines [N V] at λ 1239 Å and He II at λ 1640 Å, since the use of these lines in combination with the other carbon emission lines in the UV can be used to provide estimates of the total oxygen abundance in AGNs, as described in Dors et al. (2019). In any case, these two lines can also be used as input to the calculation of abundances in star-forming galaxies, since the presence of these lines can be considered a strong discriminating factor in the excitation of the gas when only massive stars are considered.

2.2.1 C/O derivation

Following the same procedure as defined for SF objects, the code computes C/O in a first iteration, taking advantage of the fact that the emission line ratio C3O3 depends very little on U . This observable can be defined as already used by Pérez-Montero & Amorín (2017) for star-forming galaxies to derive C/O:

$$C3O3 = \log \left(\frac{I(C\text{ III}]1909)}{I(O\text{ III}]1665)} \right) \quad (1)$$

In Fig. 1, we show the relation between this parameter and C/O for model sequences with $\alpha_{OX} = -1.2$ and assuming $f_e = 98$ per cent and grains at various $\log(U)$ at a fixed $12 + \log(O/H) = 8.7$ (left-hand panel) and for various C/O values at a fixed $\log(U) = -2.0$ (right-hand panel). We also show additional sequences of models with $\alpha_{OX} = -0.8$, with $f_e = 2$ per cent, and without dust grains to assess how varying these parameters affects this relation.

Fig. 1 shows that despite a slight dependence on O/H, U , or α_{OX} , there is a well defined linear relationship between the C3O3 parameter and C/O. Only models without grains seem to predict a slightly lower slope compared to all other sequences. Compared to the linear relation derived in Pérez-Montero & Amorín (2017) for models of star-forming galaxies, the sequences of the models for AGN are very close, albeit with a slightly lower slope, similar to that obtained for AGN without grains.

We conclude that C3O3 appears to be a robust indicator of C/O for AGN galaxies using UV emission lines, and that the code can subsequently be used for estimation.

After estimating C/O and its error, the code constrains the model grid to seek a solution for O/H and U in a second iteration. This procedure ensures that C lines can be used without any prior arbitrary assumption about the relationship between O/H and C/O if the latter can be inferred. If C/O cannot be estimated because some of the required lines are not available, the code assumes an expected relationship between O/H and C/O, as is the case for star-forming regions. By default, the code assumes a solar C/N ratio and adopts the empirical relation between O/H and N/O derived in Pérez-Montero (2014) for star-forming objects. However, in the current updated version of the code, other relationships can be considered.

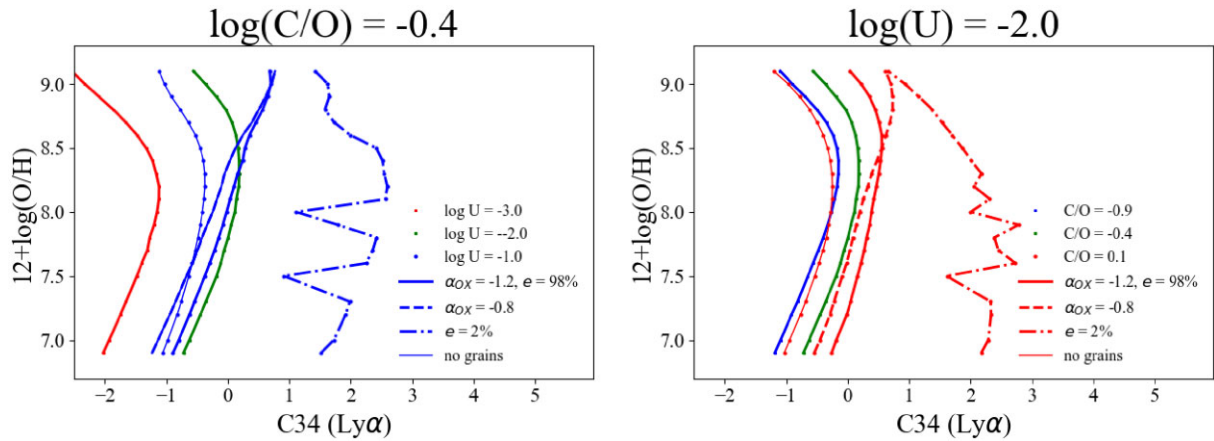


Figure 2. Relationship between emission line ratio C34 using the Ly α line and total oxygen abundance for different model series at fixed $\log(C/O) = -0.4$ (left-hand panel) and $\log U = -2.0$ (right-hand panel). The solid lines represent models for $\alpha_{OX} = -1.2, f_e$ in the outermost zone of 98 per cent and considering dust grains. The other lines change only one parameter in relation to this sequence.

2.2.2 O/H and U derivation

Among the various emission line ratios used in the second iteration to calculate the χ^2 weights, the code uses parameter C34, defined as follows:

$$C34 = \log \left(\frac{I(C\text{IV}1549) + I(C\text{III}1909)}{I(H\beta)} \right). \quad (2)$$

This parameter was also used for star-forming objects in Pérez-Montero & Amorín (2017). In this case, $I(H\beta)$ refers to the intensity of the hydrogen recombination emission lines. The closest and brightest object in this spectral range is Ly α at λ 1216 Å, but the code also allows the use of H β at λ 4861 Å, although in this last case, the extinction correction becomes much more critical.

In Fig. 2, we show the relation between this parameter, taking the Ly α intensity for the parameter, and O/H for some sequences of models from the grid at fixed $\log(C/O) = -0.4$ (left-hand panel) and $\log U = -2.0$. (right-hand panel), with $\alpha_{OX} = -1.2, f_e = 98$ per cent in the last zone and with dust grains.

It is noted that the relationship between this parameter and the total oxygen abundance in certain sequences can be bivalued, since it increases for low values of O/H, remains almost constant and finally starts to decrease when the metallicity is very high. This behaviour is in contrast to that observed in models for star-forming galaxies, where a monotonic increase in the parameter with metallicity is observed throughout the range studied, as discussed in Pérez-Montero & Amorín (2017). However, the metallicity range where the turnover of the curve is observed depends on the assumed C/O and U, and can be nearly linear for $\log U = -1.0$. In fact, these two parameters have a very large influence on the relation of the parameter to the metallicity.

Despite the large dependence of this parameter on U or C/O, the models predict a negligible deviation if we consider another harder SED with $\alpha_{OX} = -0.8$. However, the assumption of absence of dust grains seems critical, since C34 shows a much more pronounced bivalued behaviour when no grains are considered, with very lower values at high metallicities, since Ly α is much more affected by dust extinction.

In addition, the inclusion of very low excitation zones also affects the behaviour of this parameter, since Ly α is much more strongly absorbed, so that C34 is much higher for the same O/H. This is consistent with the fact that Ly α 1216 Å is often absorbed by the

neutral gas around the ionized gas nebulae and is therefore difficult to detect in many objects.

An alternative is to define the same parameter as a function of the line He II at λ 1640 Å, which is also used in Dors et al. (2019). This takes advantage of the fact that this line is often well detected with high excitation in AGN and has less absorption by the surrounding neutral gas. The corresponding observable based on the same lines can be defined as follows,

$$C34\text{He2} = \log \left(\frac{I(C\text{IV}1549) + I(C\text{III}1909)}{I(\text{He II}1640)} \right), \quad (3)$$

which is also used for the NLR of AGNs galaxies by Dors et al. (2014) named C43. However, in this work, we refer to it as C34He2 to distinguish it from our C34 parameter defined above. The relation between C34He2 and O/H depending on the model is shown in Fig. 3 for the same model series at fixed C/O = -0.4 (left-hand panel) and fixed $\log U = -2.0$ (right-hand panel) and for a value of $\alpha_{OX} = -1.2, f_e = 98$ per cent and with dust grains. Furthermore, as in the previous plots, we show additional sequences with $\alpha_{OX} = -0.8$, with $f_e = 2$ per cent in the last zone and also without dust grains.

As shown, the parameter has a similar trend to that observed for C34: it increases with increasing metallicity, although it enters saturation and begins to decrease at very high O/H values. The metallicity at which this conversion is expected to occur is so dependent on U that it is less pronounced for higher U values. This additional dependence of O/H on U strengthens the basis of the procedure in the code by which these two parameters are calculated simultaneously in this second iteration.

The relation between C34He2 and O/H does not appear to change significantly when other harder values of α_{OX} are considered and, as expected, when a larger thickness of the nebula is assumed in the models, since He II, unlike Ly α , is not absorbed by neutral gas. However, the models without grains predict much more different values of the parameter for the same O/H value, since the internal extinction of the gas affects the opacity of lines with high excitation, such as C IV or He II, leading to higher values of the parameter, in contrast to C34.

Another observable that the code can use in this second iteration is also defined and used by Dors et al. (2019) to derive O/H based on the highly excited emission lines that can be observed in the UV spectra of AGNs. It is the N5He2 parameter, which can be defined

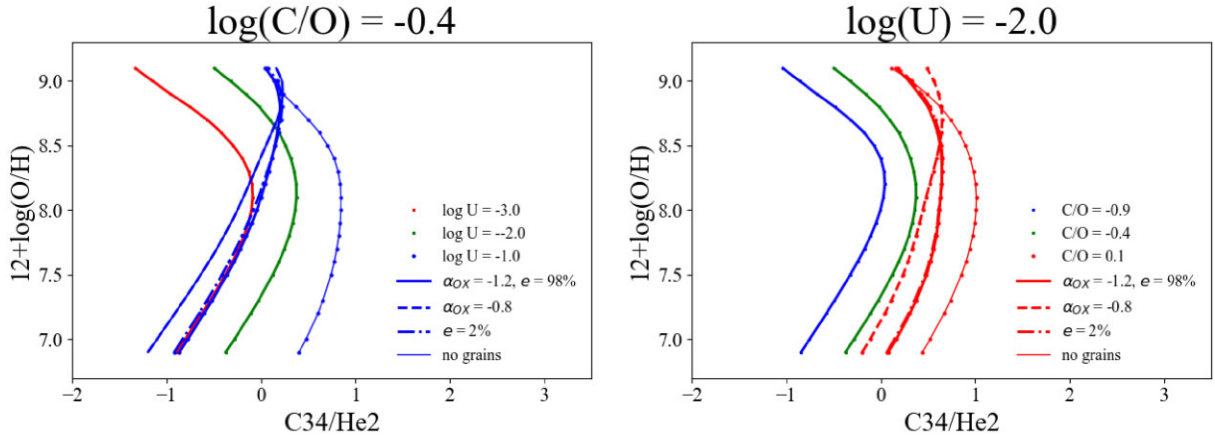


Figure 3. Relationship between C34/He2 emission line ratio and total oxygen abundance for different model sequences at fixed $\log(C/O) = -0.4$ (left-hand panel) and fixed $\log U = -2.0$ (right-hand panel). The solid lines represent models for $\alpha_{OX} = -1.2, f_e$ in the outermost zone of 98 per cent and considering dust grains. The other lines change only one parameter with respect to this sequence.

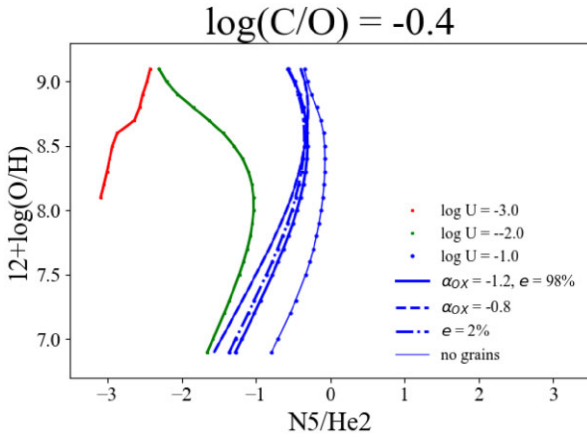


Figure 4. Relationship between the emission line ratio N5/He2 and $12 + \log(O/H)$ for model sequences with different values of the input parameters at fixed $\log(C/O) = -0.4$. The solid lines represent models for $\alpha_{OX} = -1.2, f_e$ in the outermost zone of 98 per cent and considering dust grains. The other lines change only one parameter with respect to this sequence. The dashed line represents models with $\alpha_{OX} = -0.8$, the dot-dashed line represents models with f_e of 2 per cent, and the thin line represents models without grains.

as follows,

$$N5He2 = \log \left(\frac{I([NV]1239)}{I(He\ II\ 640)} \right). \quad (4)$$

In Fig. 4, we show the relation between this parameter and O/H for model sequences at fixed $C/O = -0.4$ and varying $\log U$, assuming an AGN SED with $\alpha_{OX} = -1.2$, a final zone with $f_e = 98$ per cent, and grains. Additional sequences also consider other values for these input parameters.

Similar to C34 and C34He2, the N5He2 parameter also shows a strong dependence on U and a bivalued relationship with oxygen abundance. The parameter has a lower value for lower U , but on the contrary, it does not appear to change the metallicity of the turnover point.

Moreover, since it depends on the lines with high excitation, it is more sensitive to the shape of SED, so it has lower values when we vary $\alpha_{OX} = -0.8$ and does not change significantly for a lower value of f_e in the last zone of the models. Finally, the absence of

dust grains is not negligible, but the difference is not as large as in the case of C34, due to the same cause. Moreover, since N is also a secondary element, N5He2 has a strong dependence on N/O, which can be partially reduced by assuming that C/N remains unchanged in the models, although this is not fully justified since the stellar mass range of the nucleosynthetic production of these two elements is not exactly the same (Henry, Edmunds & Köppen 2000), but can be similarly affected by processes of hydrodynamic gas exchange (Edmunds 1990). Changing N/O independently of C/O, in the grids of models, would allow us in principle to explore in more detail the impact of N/O on the final metallicity derivation, but the absence of any UV emission-line ratio strictly dependent on N/O, does not allow us to incorporate it to the code and would unnecessarily enlarge the number of models in each grid.

As commented, the dependence on C/O of the emission line ratios defined above to derive O/H can be reduced by the prior determination of C/O in the first iteration using the C3O3 parameter. As for the excitation, the dependence of the various observables on it can also be reduced by the C3C4 emission line ratio defined as follows,

$$C3C4 = \log \left(\frac{I(C\ III\ 1909)}{I(C\ IV\ 1549)} \right). \quad (5)$$

This ratio is already used by the code for star-forming objects and also by Dors et al. (2019) for the case of NLRs in AGNs. This ratio was already proposed by Davidson (1972) as an indicator of excitation in gas nebulae, although Dors et al. (2014) point out that it also depends on metallicity for low values of $\log U$.

The relation of this emission line ratio with the ionization parameter is shown in Fig. 5 for different arbitrary model sequences at fixed $\log(C/O) = -0.4$ (left-hand panel) and fixed $12 + \log(O/H) = 8.7$ (right-hand panel) and assuming $\alpha_{OX} = -1.2, f_e = 98$ per cent and with grains. As in the previous cases, models with harder SED are also shown with $\alpha_{OX} = -0.8$, with $f_e = 2$ per cent and also without grains in the figures.

As can be seen, higher values of C3C4 indicate lower values of U for most sequences, except for very high values of O/H, which show a bivalued behaviour. This is a weaker effect compared to the relationship found for the O32 parameter for AGNs using the same models in the optical (Pérez-Montero et al. 2019), which exhibits bivalued behaviour at all values of O/H with a maximum value for $\log U = -2.5$. This monotonically decreasing relationship between

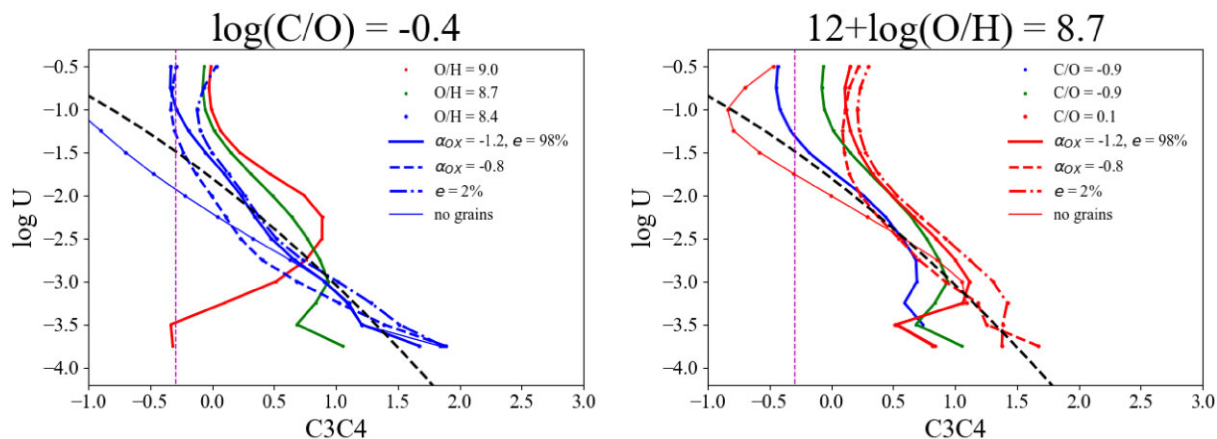


Figure 5. Relationship between emission line ratio C3C4 and ionization parameter for different model sequences at fixed $\log(C/O) = -0.4$ (left-hand panel) and fixed $12 + \log(O/H) = 8.7$ (right-hand panel). The solid lines represent models for $\alpha_{OX} = -1.2$, the ratio of free electrons in the outermost zone of 98 per cent and considering dust grains. The other lines change only one parameter with respect to this sequence; the black dashed line represents the quadratic fit of Dors et al. (2019). The vertical dashed magenta line marks the distance assumed for the C3C4 parameter to account for dust in the models for subsequent analysis.

C3C4 and U makes it easier for the code to use the grid of models for all values of U . This trend does not change noticeably when we consider a value for $\alpha_{OX} = 0.8$ or a lower f_e for the termination criterion.

On the other hand, the C3C4 parameter is very sensitive to the presence of dust grains mixed with the gas. Neglecting the presence of dust in the models results in much lower values for C3C4. Indeed, the relationship that emerges from these models without dust is similar to the quadratic fit of Dors et al. (2019), where the authors do not consider dust grains in their models. For this reason, some authors, such as Nagao et al. (2006) or Dors et al. (2019), do not include dust in their models because many of the analysed objects have very low values of C3C4. However, according to the model sequences shown in Fig. 5, models with dust cannot be excluded for values of the C3C4 parameter > -0.3 , a threshold marked with a red line in the left-hand panel of the figure. In any case, other possible explanations for this very low values of C3C4 cannot be excluded and deserve future investigation, such as the possible existence of photon leaking, already observed in some extreme star-forming galaxies (e.g. Schaerer et al. 2022).

2.3 Testing the method with model emission lines

To verify the results of our model-based method, we used as input to the code the same emission line intensities predicted by the models to check that we obtain the same chemical abundances and ionization parameters used for them. For this purpose, we also included a 10 per cent uncertainty in the predicted model-based fluxes to simulate the effect of an additional source of error on the estimates. As explained above, the code uses the error of the flux as the standard deviation of a normal distribution of cases around the nominal value to perform a series of iterations that also reveal the associated uncertainty in the results.

In the panels of the first row in Fig. 6, we show the input abundances and U assumed in the models of the grid for $\alpha_{OX} = -1.2$, a termination criterion when $f_e = 98$ per cent is reached, and with dust grains. These values are compared with the results of the HCM-UV code when the same conditions are assumed and all lines accepted by the code are used. As can be seen, the agreement is excellent for most of the studied ranges (i.e. both the mean offset and the standard deviation of the residuals are less than 0.01 dex), so that

both the abundances and the $\log(U)$ values can be determined using only the emission line intensities. Only for $12 + \log(O/H) < 7.5$ does the code tend to find solutions that are about 0.1 dex above the correct input value for each model, but still within the error limits (i.e. 0.17 dex). For very high values of $\log(U)$ (i.e. > -0.8), the code also tends to find results that are below the correct values, with deviations greater than the errors obtained (with a mean of 0.2 dex), but for the rest of the examined range, there is agreement that is better than the associated errors.

We also investigate the potential impact in the results of changing the assumed conditions in the library used by HCM-UV. Thus, we ran the code assuming the same conditions as above, but using as input the emission lines predicted by the models when we assume a value $\alpha_{OX} = -0.8$, and leaving the other parameters equal to those assumed by the code. The corresponding comparisons are shown in the second line of Fig. 6. In the case of O/H, the mean deviation is larger than the median uncertainty (0.18 dex) only at very low values, although there is also a systematic deviation for $O/H > 8.0$, in the sense that the code determines O/H values that are 0.1–0.2 dex below the correct values. In contrast to O/H, the mean deviation for C/O is always lower than the obtained uncertainty (0.11 dex) in all ranges. This confirms that C/O can be determined more reliably than O/H when a different ionizing SED is assumed. However, the U estimate is more affected by the shape of the SED as it is significantly overestimated, especially in the range $-3 < \log U < -1$.

In the third line of Fig. 6, we show the comparisons when we change the truncation criterion in the models used as input to a fraction of free electrons = 2 per cent and leave the other parameters the same. Opposite to the input, the code still considers the same conditions as those assumed in the first case (i.e. with 98 per cent fraction of free electrons in the last model). In this case, when the code assumes a different higher f_e value, the main offset occurs at high O/H values, where the code finds solutions about 0.3 dex below the correct input value, proving the importance of the relative intensity of the H I lines to derive metallicity. On the other hand, no large deviation is found for the C/O derivative, but in the case of U the code systematically finds much lower values for $\log U > -1.0$.

Finally, in the bottom row of Fig. 6, we show the comparisons between the input values for models that do not consider dust and the values derived by the code assuming dust is present. As shown, in this situation, the code overestimates O/H with a mean offset

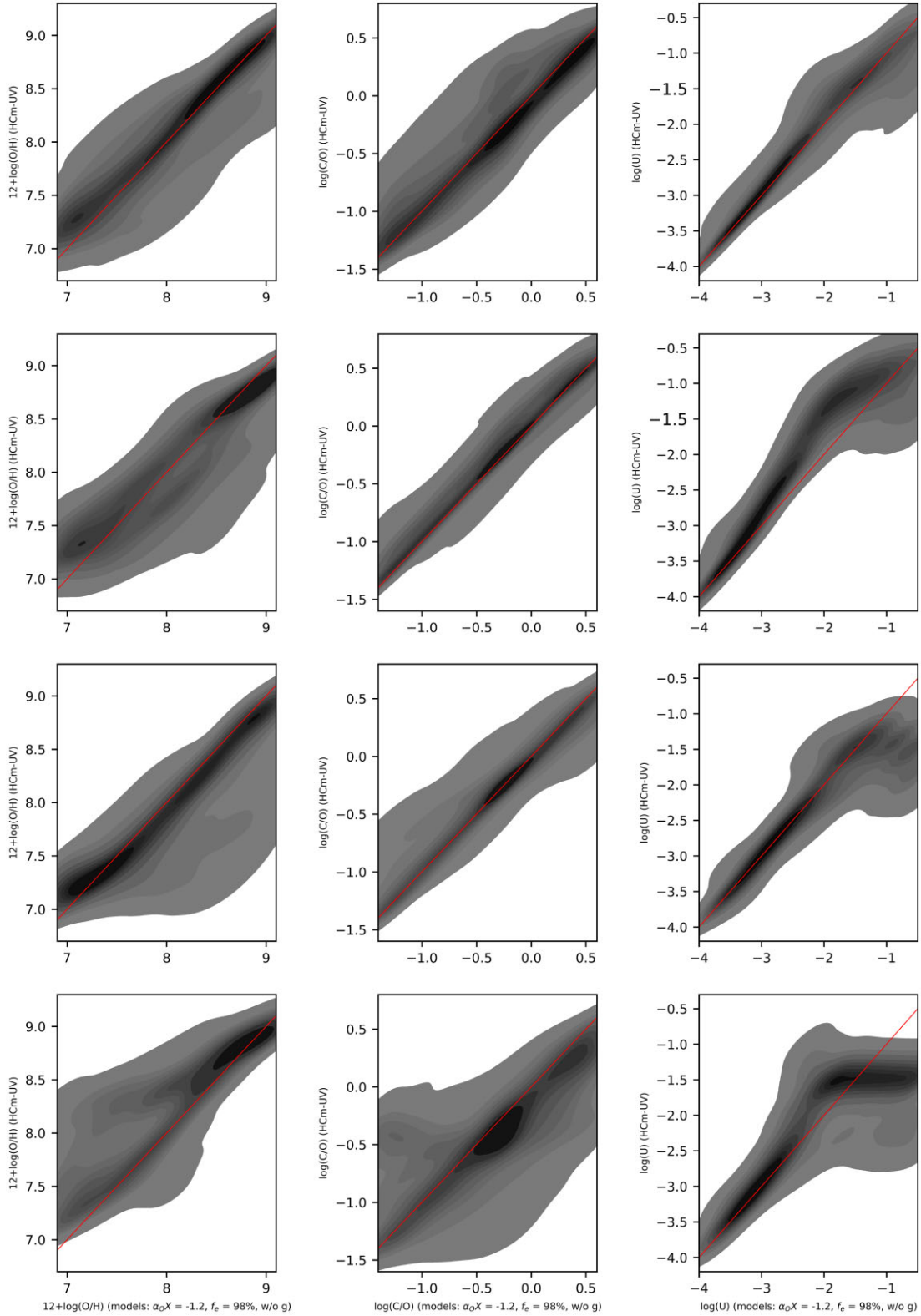


Figure 6. Comparisons between the chemical abundances and U assumed in the model grid and the same quantities calculated by HCM-UV when the predicted emission lines are used as input. The panels in the left column show the comparison for $12 + \log(\text{O}/\text{H})$, the middle column for $\log(\text{C}/\text{O})$, and the right column for $\log U$. In all cases, HCM-UV AGN models with $\alpha_{\text{OX}} = -1.2$, $f_e = 98$ per cent and considering grains. In the panels of the first row, we show the results when the same conditions are assumed for the input; in the second, we change α_{OX} to -1.2 ; in the third row, we consider $f_e = 2$ per cent; and finally, in the bottom row, without dust grains. The solid red line represents the 1:1 relation in all panels.

Table 1. Median deviations and root mean squares (RSME) of residuals between theoretical abundances and $\log(U)$ values (AGN model inputs) and estimates from HCM-UV using different sets of emission lines and for different grids.

Set of lines	Models	Δ_{OH}	RSME _{OH}	Δ_{CO}	RSME _{CO}	Δ_U	RSME _U
All lines	All	+0.01	0.21	+0.02	0.14	−0.01	0.26
Ly α , N v], C IV], He II, O III] λ 1665 Å, C III]	All	+0.08	0.25	−0.05	0.14	+0.03	0.11
N v], C IV], He II, O III] λ 1665 Å, C III]	All	+0.08	0.25	−0.05	0.14	+0.03	0.11
N v], C IV], He II, C III]	All	+0.36	0.57	–	–	+0.11	0.34
N v], C IV], He II, C III]	O/H/C/O const.	+0.01	0.15	–	–	+0.01	0.13
C IV], He II, C III]	All	+0.32	0.64	–	–	+0.04	0.46
C IV], He II, C III]	O/H/C/O const.	+0.03	0.33	–	–	−0.03	0.31
N v], He II	All	+0.27	0.66	–	–	+0.08	0.48
N v], He II	O/H/C/O const.	+0.00	0.52	–	–	−0.00	0.42

larger than the mean uncertainty (i.e. 0.17 dex) for $O/H < 8.0$, but underestimates it for $O/H > 8.5$, albeit with a large spread in each case. For C/O , the deviation between the solutions and the theoretical values is always within uncertainty (about 0.2 dex), except for very low values for C/O . It is also noted that there is a systematic tendency to find higher C/O values for high input values of C/O , but these deviations are always within errors. Finally, in the case of U , we find better agreement, although the deviations are large for the highest values of U .

From these comparisons, it appears that the C/O ratio is more robust than the O/H ratio when the assumed conditions in the models vary relative to those assumed by the code. In the case of O/H , this is especially the case at high metallicities when the assumption about the presence of dust grains is incorrect, while for U , the largest discrepancies are found at very high values in all the comparisons tested. Finally, for $\log U < -1.5$, all discrepancies are found within the derived uncertainties.

2.4 Results as a function of different sets of input emission lines

Another important aspect in the evaluation of our code arises from the fact that it can provide solutions for different sets of emission lines. To this end, in this subsection, we compare the theoretical and resulting abundances, again using as inputs to the code different sets of emission line fluxes with an additional 10. The corresponding mean offsets and standard deviation of the residuals obtained from the code for O/H , C/O , and $\log U$ compared to the theoretical values assumed by the models are shown in Table 1, for different combinations of emission lines that can be given as input to the code, and for different constraints on the model grid used.

As shown, when all lines allowed by the code are specified, the mean offsets of the results are better than the mean scatter in all cases. This comparison is the same as that in the first line of Fig. 6. This comparison is slightly worse when the optical line [O III] at λ 5007 Å, which is allowed by the code relative to O III] λ 1665 Å is not provided, but the results still agree better than the associated uncertainties. A similar result is obtained if the emission line Ly α at λ 1216 Å is removed, since He II can be used instead. This has no influence on the C/O determination.

On the other hand, if the O III] λ 1665 Å is not provided, HCM-UV cannot calculate the $C3O3$ ratio for the C/O estimate. In this case, very large deviations and errors result for both O/H and $\log U$ when the full model grid is used for calculation. In this scenario, the code must assume a certain O/H – C/O ratio to get a better solution for O/H when C-lines are used. As shown in Table 1, both the mean offsets and the standard deviation for O/H and $\log U$ are much better under this additional assumption. However, it is important to remember

that this relation may be somehow arbitrary or valid for a particular galaxy population and not valid for a particular object. In any case, even assuming such a relationship in the absence of the lines required for the previous derivation of C/O , much better results are obtained if the lines C III], C IV], and N v] are used simultaneously with respect to He II rather than calibrating them individually and in combination.

The above results again highlight the importance of a prior determination of the C/O content in order to obtain an accurate determination of the total metal content of the gas, and are in agreement with the results already obtained using the same approach for star-forming galaxies in Pérez-Montero & Amorín (2017).

3 APPLICATION TO GALAXY SAMPLES

We compiled from the literature strong UV narrow emission line fluxes for a sample of AGN consisting of Seyferts 2 (10), quasars (33), quiet radio galaxies (2), high- z AGN (1), and high- z radio galaxies (96). We take advantage of previous compilation work, (e.g. Nagao et al. 2006; Dors et al. 2019) of strong UV emission lines in AGN, namely N v λ 1239 Å, C IV λ 1549 Å, He II λ 1640 Å, and C III] λ 1909 Å, but we also include information on the Ly α and [O III] λ 1665 Å emission lines when their measurements are given in the original references. Table 2 shows all the information we found for our sample, as well as the original references.

The Seyferts 2 (S2) sample consists of 9 objects taken directly from Nagao et al. (2006) and one additional galaxy, IZw 92, from Kraemer et al. (1994b). The sample of high- z radio galaxies (HZRG) was taken directly² from the compilation presented by De Breuck et al. (2000), supplemented by 8 sources observed by Bornancini et al. (2007) and 9 galaxies analysed by Matsuoka et al. (2009). Our sample of quasars (QSO) consists of three different types of galaxies: Type II type quasars (11), 10 of them listed by Nagao et al. (2006) plus J142331.71–001809.1, recently analysed by Onoue et al. (2021); extremely red quasars (21) from the compilation of Villar Martín et al. (2020); and one intermediate Type I–II quasar, observed by Lin et al. (2022). We added to the above list of objects 2 quiet radio galaxies (QRG) observed by Matsuoka et al. (2018), and a high- z AGN (zAGN) whose broad and narrow components were identified by Tang et al. (2022).

Some of the compiled observations were already corrected for Galactic extinction in the original publications. These corrections were not very large [i.e. $E(B - V) \sim 0.01$ – 0.1] due to their relative position on the sky, and do not lead to changes in the resulting

²From the original list of 167 sources, we omit nine sources observed by Matsuoka et al. (2009) that provide better accuracy, and 79 sources that do not have enough UV spectroscopic information to be used as input to HCM-UV.

Table 2. List of UV fluxes for our sample of AGN.

Name (1)	z (2)	Type (3)	Ly α (4)	Nv1239 Å; (5)	Civ1549 Å; (6)	HeII1640 Å; (7)	OIII]1665 Å; (8)	CIII]1908 Å; (9)	Ref. (10)
NGC 1068	0.004	S2	713 ± 100	224 ± 41	520 ± 80	187 ± 29	22 ± 8	240 ± 35	NA06,SNI86
I ZW 92	0.029	S2	121.2 ± 40.3	–	25.2 ± 8.4	3.84 ± 1.28	–	–	KRA94
CDFS-901	2.578	QSO	$3.71e^{-3} \pm 6e^{-5}$	$6.5e^{-4} \pm 8e^{-5}$	$1.97e^{-3} \pm 1e^{-4}$	$1.87e^{-4} \pm 9.3e^{-5*}$	–	$3.3e^{-4} \pm 9e^{-5}$	NA06,SKO04
CXO52	3.288	QSO	$1.89e^{-2} \pm 4e^{-4}$	$6e^{-4} \pm 1.2e^{-4}$	$3.5e^{-3} \pm 2e^{-4}$	$1.7e^{-3} \pm 2e^{-4}$	$9e^{-5} \pm 3e^{-5}$	$2.1e^{-3} \pm 2e^{-4}$	NA06,STE02
S82-20 ¹	3.062	QSO	36.10 ± 0.21	1.34 ± 0.12	8.67 ± 0.05	1.52 ± 0.04	0.38 ± 0.04	2.04 ± 0.04	LIN22
TXS J2334+1545	2.480	HZRG	$3.1e^{-2} \pm 5e^{-3}$	$7e^{-4} \pm 3e^{-4*}$	$1e^{-3} \pm 1e^{-3}$	–	–	$8e^{-3} \pm 3e^{-3}$	BRE00,BRE01
TN J1941-1951	2.667	HZRG	$3.7e^{-2} \pm 4^{-3}$	–	$9e^{-3} \pm 1e^{-3}$	$4e^{-3} \pm 1e^{-3}$	–	$2e^{-3} \pm 1e^{-3}$	BOR07
COSMOS 05162	3.524	QRG	$7.68e^{-2} \pm 1.3e^{-3}$	$3.89^{-3} \pm 1.95e^{-3*}$	$1.19e^{-2} \pm 8e^{-4}$	$2.6e^{-3} \pm 3e^{-4}$	–	$4.05e^{-2} \pm 6.5e^{-3}$	MAT18
COSMOS 10690	3.100	QRG	$8.1e^{-3} \pm 4.1e^{-3*}$	$4.5e^{-3} \pm 2.3e^{-3*}$	$2.25e^{-3} \pm 6.8e^{-4}$	$8.2e^{-4} \pm 4.1e^{-4*}$	–	$1.7e^{-3} \pm 5e^{-4}$	MAT18

Note. Column (1): name of the galaxy. Column (2): redshift. Column (3): spectral type. Columns (4)–(9): UV emission line fluxes and their errors in $1e^{-14}$ erg s^{-1} cm $^{-2}$. Column (10): references: AS88 (Allington-Smith et al. 1988), BER81 (Bergeron, Maccararo & Perola 1981), BES99 (Best, Röttgering & Lehnert 1999), BES00 (Best, Röttgering & Longair 2000), BOR07 (Bornancini et al. 2007), BRE00 (De Breuck et al. 2000), BRE01 (De Breuck et al. 2001), CIM98 (Cimatti et al. 1998), GK95 (Gopal-Krishna et al. 1995), KI93 (Kinney et al. 1993), KRA94 (Kraemer et al. 1994a), LAC94 (Lacy et al. 1994), LAC99 (Lacy et al. 1999), LIL88 (Lilly 1988), LIL07 (Lilly et al. 2007b), LIN22 (Lin et al. 2022), MAL83 (Malkan & Oke 1983), MAT09 (Matsuoka et al. 2009), MAT18 (Matsuoka et al. 2018), MCC90 (McCarthy et al. 1990a), MCC90b (McCarthy et al. 1990b), MCC91 (McCarthy 1991), MCC91b (McCarthy et al. 1991), NA06 (Nagao et al. 2006), ONO21 (Onoue et al. 2021), RAW96 (Rawlings et al. 1996), ROB88 (De Robertis, Hutchings & Pitts 1988), ROT97 (Roettgering et al. 1997), SIM99 (Simpson et al. 1999), SNI86 (Snijders, Netzer & Boksenberg 1986), SPI95 (Spinrad, Dey & Graham 1995), STE99 (Stern et al. 1999), STE02 (Stern et al. 2002), SZO (Szokoly et al. 2004), TAN22 (Tang et al. 2022), THU84 (Thuan 1984), VM99 (Villar-Martín et al. 1999), VM20 (Villar Martín et al. 2020), WAD99 (Waddington et al. 1999). * stands for emission lines provided by their upper limit.¹Emission lines given as luminosity in units 10^{43} erg s^{-1} . The complete version of this table is available at the CDS.

emission-line fluxes larger than the error limits. On the other hand, we assumed that these objects were not corrected for internal extinction, so we performed this correction only for those objects with C3C4 > –0.3, which cannot be considered as dust free. This criterion, shown in Fig. 5, is consistent with the predictions from models in which the absence of internal extinction is the only way to achieve the very low C3C4 values observed for certain objects (Nagao et al. 2006; Dors et al. 2019). For higher C3C4 values, on the other hand, the absence of extinction does not seem to be justified in either the emission line flux correction or the photoionization models. Therefore, for the rest of the compiled galaxies, we assumed an average visual extinction of $A_V = 1$ mag and an extinction law of Cardelli, Clayton & Mathis (1989). Anyway, we checked that the assumption of other common extinction laws does not imply a variation in the resulting chemical abundances larger than the reported errors when only UV emission lines are used as an input, as in our sample. For the case of a simultaneous use of both optical and UV lines, this correction would be more critical, but a more accurate estimate of the extinction correction could also be performed using the Balmer decrement.

Some of the listed fluxes for faint emission lines (e.g. N v λ 1239 Å, [O III] λ 1665 Å) are given as upper limits (noted in Table 2). However, they are treated as real lines, assuming the upper limit equivalent to 3σ , where the code considers as input the flux with a nominal value of 2σ with an error of 1σ (i.e. an upper limit of 3 is introduced as 2 ± 1), to reduce the probability that they are just noise, although with a restriction for values > 3σ (i.e. larger than the upper limit) in our Monte Carlo simulations).

We applied the HCM-UV code to this sample, assuming an AGN SED with $\alpha_{OX} = -1.2$ and a stopping criterion in the models for $f_e = 98$ per cent. The choice of these input parameters is arbitrary and corresponds mainly to the same conditions used for the optical version of the code in Pérez-Montero et al. (2019), with an α_{OX} value closer to the median derived by Miller et al. (2011). Anyway, the effects of changing these parameters on the results are discussed in Section 2. The only difference is that we only considered dust in the models for the objects whose lines were corrected for internal extinction, in agreement with the criterion based on C3C4, while for the rest, we used only the grids of the models without dust. The

resulting O/H, C/O, and log U values are provided in electronic form along with the corresponding derived errors, as shown in Table 3.

4 DISCUSSION

4.1 O/H and U distributions

In Fig. 7, we show the derived metallicity in the compiled sample as a function of redshift for the objects marked for different categories. We see no clear correlation with redshift, but a large scatter in the range of metallicity $7.77 < 12 + \log(O/H) < 8.97$, with a mean of 8.52 ($\sim 2/3 Z_{\odot}$), which is slightly higher for the objects assumed to be dusty (i.e. 8.55) than for the objects we assume to be dust free (8.46). The main trend observed in this distribution would not be then very different assuming different input conditions in the models chosen to derive the abundances.

In Table 4, we show the mean O/H values obtained for each galaxy class. While these values do not allow us to draw firm conclusions, since these types are very unevenly populated and some of them could be very heterogeneous in their properties, they can provide some clues. For example, at very low z , Seyfert-2 galaxies have abundances around the mean of the whole sample, even if their mean is slightly subsolar. This is almost congruent with the sample of radio galaxies at high z , whose mean redshift is higher than that of the smaller Seyfert 2 subsample. On the other hand, for the other types of galaxies at high z , very different values of O/H are found, as in the case of quasars, with a mean O/H value significantly lower [i.e. $12 + \log(O/H) = 8.35$] than the mean of the whole sample. However, for the other three defined classes, the number of compiled objects is so small that no statistically significant conclusion can be drawn.

In Fig. 8, we show the relationship between the C3C4 parameter as obtained from the compiled emission line fluxes and the value of log U as obtained from HCM-UV. As described in previous sections, we considered all objects with C3C4 < –0.3 to be possibly dust free, as discussed by Nagao et al. (2006) or Dors et al. (2019). In Table 4, we also give the fraction of objects in each category that fall within

Table 3. Chemical abundances estimated from HCM-UV, using the grid of AGN models for $\alpha_{OX} = -1.2$ and the stopping criteria of 98 per cent of free electrons. Dust-free or grain-included models are selected based on their C3C4 value.

Name (1)	$12 + \log(\text{O}/\text{H})$ (2)	$\log(\text{C}/\text{O})$ (3)	$\log(U)$ (4)	Grains (5)
NGC 1068	8.30 ± 0.31	-0.08 ± 0.34	-1.04 ± 0.16	No
I ZW 92	–	–	–	–
CDFS-901	8.78 ± 0.15	–	-1.12 ± 0.08	No
CXO52	7.79 ± 0.26	0.24 ± 0.26	-1.39 ± 0.21	Yes
TXS J2334+1545	8.82 ± 0.10	–	-2.61 ± 0.16	Yes
TN J1941–1951	8.56 ± 0.14	–	-1.29 ± 0.27	No
COSMOS 05162	8.77 ± 0.14	–	-1.16 ± 0.16	No
COSMOS 10690	8.68 ± 0.09	–	-0.84 ± 0.11	Yes

Note. Column (1): name of the galaxy. Column (2): oxygen abundance (O/H) and its uncertainty. Column (3): carbon-to-oxygen (C/O) abundance ratio and its uncertainty. Column (4): ionization parameter (U) and its uncertainty. Column (5): whether grids of models accounting for grains are employed. The complete version of this table is available at the CDS.

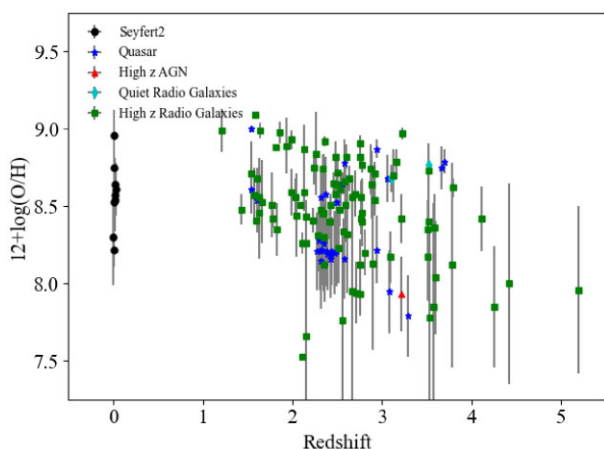


Figure 7. Relationship between redshift and total oxygen abundances derived with the HCM-UV. Different symbols represent different object types in the sample: black circles for Seyfert 2, blue stars for quasars, red triangles for high- z AGN, cyan diamonds for quiet-radiogalaxies, and green squares for high- z radio galaxies.

this range. As can be seen, more than half of the compiled objects in all categories are in this range and, could have in principle no dust, except for the radio galaxies with high z .

As for U , we find a relatively wide range of values from $-2.7 < \log U < -0.6$ with a mean $\log U = -1.4$, indicating that most objects have high excitation. Although we find a clear correlation between C3C4 and $\log U$, the objects assumed to not to have dust do not have a higher mean U than the objects with dust. This is a consequence of the models predicting a lower C3C4 value in the absence of dust in order to obtain the same U value.

In Table 4, we also report the mean $\log U$ value in each category, which for Seyfert 2, as in the case of O/H, is very similar to the average values of the whole sample. In contrast, quasars show a much higher mean value, while radio galaxies with high z show lower ionization parameters on average.

4.2 C/O and its impact on the O/H derivation

For those objects in the sample for which the emission line ratio C3O3 was available, the code also estimated C/O. Unfortunately, the number of objects in our sample for which this ratio is measurable is

small (i.e. only 26 objects), most of which are quasars with an upper limit on the O III] λ 1665 Å line measurement, which could mean that the derived C/O values are only lower limits. In Table 4, we also report the mean C/O values for each category, although they are not statistically significant for most classes because they could not be derived for many objects.

In Fig. 9, we show the resulting O/H and C/O values with the corresponding errors for the objects for which these two ratios could be estimated simultaneously. We note that most of the objects for which C/O could be derived have similar properties, since most of them are quasars all containing dust (according to the C3C4 criterion) and have relatively low O/H abundances in the range of $7.83 < 12 + \log(\text{O}/\text{H}) < 8.31$. The resulting C/O values for this subsample are in the range $-0.84 < \log(\text{C}/\text{O}) < 0.27$, with a mean of -0.50 ($\sim 0.6 (C/O)_{\odot}$), a somewhat lower proportion relative to the solar value than the corresponding O/H value for the entire sample, but significantly higher when compared to the mean for the subsample for which C/O could be measured ($12 + \log(\text{O}/\text{H}) = 8.17 \sim 0.3 Z_{\odot}$).

This relatively higher mean C/O value compared to the corresponding derived O/H value results in this subsample being on average above some of the commonly assumed relationships between O/H and C/O, as shown in Fig. 9. The sample is well above the relations given by Hamann & Ferland (1993) or Dopita et al. (2006), and only a fraction of the objects are in the range considered by Pérez-Montero & Amorín (2017), remembering that the latter is only the conversion of the O/H–N/O relation assuming a solar C/N abundance ratio. It is not uncommon to find low-emission objects above these empirical or chemical model-based relations, since the relationship between metallicity and the ratio of abundance with a partial secondary origin relative to another with a primary origin has a large scatter (e.g. Pérez-Montero & Contini 2009). The origin of such a scatter is related to several processes, including variations in star formation efficiency (Mollá et al. 2006) or gas exchange between galaxies and the surrounding IGM through hydrodynamic processes (Edmunds 1990; Köppen & Hensler 2005), which likely affect the NLR in AGNs. This highlights the need for an alternative method to derive more accurate O/H abundances using UV carbon lines based on prior determination of C/O.

Indeed, the lack of prior determination of the C/O abundance ratio is one of the main sources of uncertainty we find in deriving chemical abundances from UV lines in both star-forming objects and AGN. In the absence of an emission line ratio sensitive to electron temperature, the calculation is based on the measured flux ratio of C III] and C IV

Table 4. Mean resulting values obtained from HCM-UV for O/H, C/O, and $\log U$ in our sample of objects as a function of the galaxy type. We also list the mean redshift and the number of galaxies for which the calculation could be done to derive O/H and C/O, and the number of objects without dust grains.

Galaxy type	mean z	N_{OH}	N_{wg}	Mean O/H	Mean $\log U$	N_{CO}	Mean C/O
All	2.41	139	56	8.52	-1.48	26	-0.50
Seyfert 2	0.015	9	6	8.56	-1.40	1	0.06
Quasar	2.51	32	20	8.35	-1.16	23	-0.53
high- z radio galaxies	2.57	95	24	8.56	-1.65	1	-0.51
High- z AGN	3.21	1	1	8.03	-1.44	1	-0.27
Quiet radio galaxies	3.31	2	1	8.84	-1.04	0	-

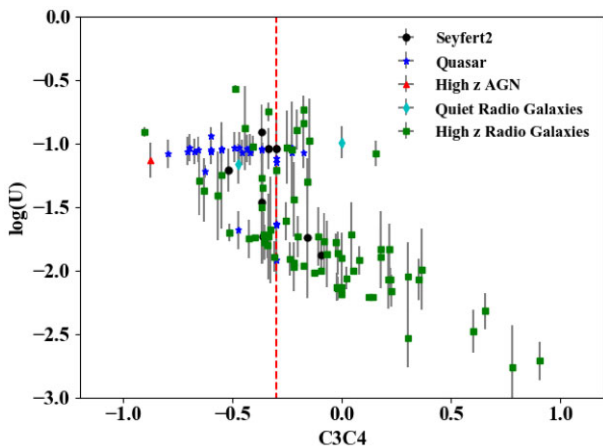


Figure 8. Relation between the C3C4 parameter and the ionization parameter, $\log(U)$, as derived using HCM-UV for our sample of objects. The different symbols are the same as in Fig. 7. The vertical red dashed line marks the limit below which objects are considered not having dust.

lines relative to Ly α or He II λ 1640 Å. The code HCM-UV for star-forming objects presented in Pérez-Montero & Amorín (2017) and the fit for AGNs presented in this work performs an initial iteration through the entire grid of assumed models to search for C/O using the observed C3O3 ratio, but we may wonder to what extent the derived final O/H values may vary if this previous step cannot be performed.

We recalculated all O/H abundances in the subsample of 29 galaxies for which a prior derivation of C/O was possible, but this time without considering the O III] λ 1665 Å line. The latter means that the code cannot compute C/O and instead assumes the a priori expected relationship between O/H and C/O. In this case, we obtain a mean O/H value of 8.66, which is 0.47 dex larger than the value obtained with a previous C/O derivation. Since most of the objects in our sample are quasars, the significantly lower O/H value derived for this category (see Table 4) could have the origin explained above, and similar lower values cannot be discarded if an estimate of C/O can be given for the other object classes.

We also computed the O/H frequency assuming a restricted grid, taking the relationship between O/H and C/O proposed by Dopita et al. (2006) as a reference, since the new version of the code allows easy manipulation of this relationship, and we obtain an even larger mean frequency of 8.71. The 0.05 dex difference between the O/H frequencies derived from HCM-UV when the program assumes the relationship given by Pérez-Montero & Amorín (2017) or the relationship given by Dopita et al. (2006) or Hamann & Ferland (1993) in the absence of a prior C/O determination is also obtained for the entire object sample.

In summary, the very large variation between metallicities derived using C-lines from UV with or without prior C/O determination underscores the importance of measuring the C3O3 parameter to obtain accurate O/H abundances.

4.3 Comparison with other calibrations

We use our sample to compare the total oxygen abundances and $\log U$ derived from HCM-UV with the results obtained with the model-based calibrations for AGNs with UV emission lines proposed by Dors et al. (2019).

In the left-hand panel of Fig. 10, we show the comparison for O/H obtained using the biparametric function proposed by Dors et al. (2019), which is based on the combination of the C34He2 parameter with a correction of its dependence on U using C3C4. We find agreement within the errors, both for objects with and without dust. Only for very large abundances ($12 + \log O/H > 9.0$) do we find a larger deviation due to the limit on HCM-UV (i.e. the maximum O/H value is 9.1).

Conversely, we find poor agreement when we compare the results of HCM-UV with the abundances resulting from calibration based on N5He2 and C3C4 in Dors et al. (2019), shown in the middle panel of Fig. 10. As can be seen, the agreement is not good, and neither a clear correlation nor the range covered is similar for the two approaches. These strong observed differences cannot be attributed solely to the use of models with or without dust grains or to the assumption of different relationships between O/H and C/O, since these facts do not lead to such large differences, as discussed above. Instead, as we show in Table 1, they may be due to independent use of C III], C IV], and N V] relative to He II. Therefore, these results reaffirm the conclusion that the use of the N5He II parameter alone is not advisable, but that, on the contrary, it must be used in combination with the other UV carbon lines.

In summary, the O/H derivation using these lines leads to very different results, even when the three lines are used and a C/O estimation was previously performed. For the sample of 26 galaxies with a prior determination of C/O using the C3O3 parameter, the mean difference between the O/H values obtained from HCM-UV and the calibrations using the C34he2 and N5He2 parameters from Dors et al. (2019) is -0.2 and -0.9 dex, respectively. In contrast, better agreement is obtained when $\log U$ is derived using the C3C4 emission line ratio, as shown in the right-hand panel of Fig. 10, which has an average offset of only 0.04 dex.

4.4 Comparison with optical-based estimations

Finally, we can compare the chemical abundances obtained from HCM-UV using UV emission lines with those derived using optical emission lines from the version of the code described in

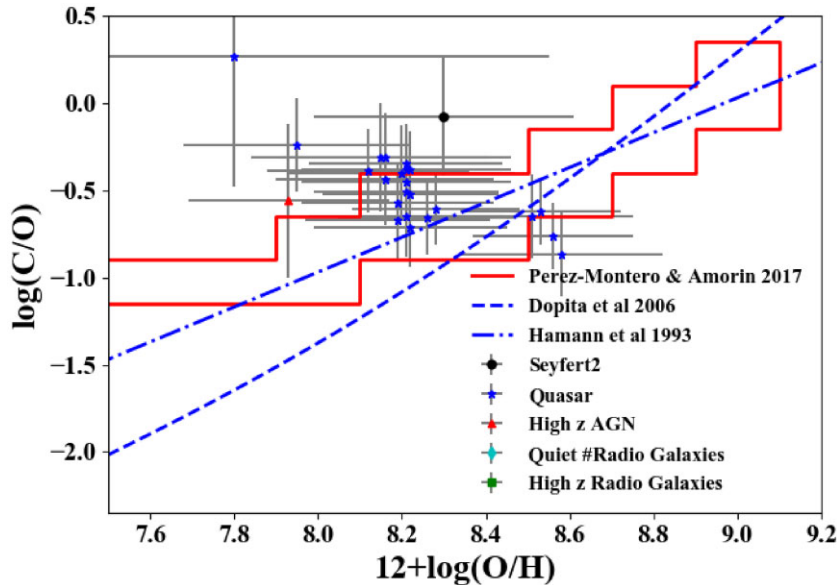


Figure 9. Relationship between total oxygen abundance and carbon–oxygen abundance ratio derived using HCM-UV for the assembled sample of NLR in AGN. The red solid line encompasses the range covered by the models when the code in Pérez-Montero & Amorín (2017) assumes no prior derivation of C/O and a prior assumption about the ratio of O/H to C/O is required. The blue dashed line corresponds to the relationship derived by Dopita et al. (2006) for H II regions, and the dashed blue line represents the relationship derived by Hamann & Ferland (1993) for QSOs.

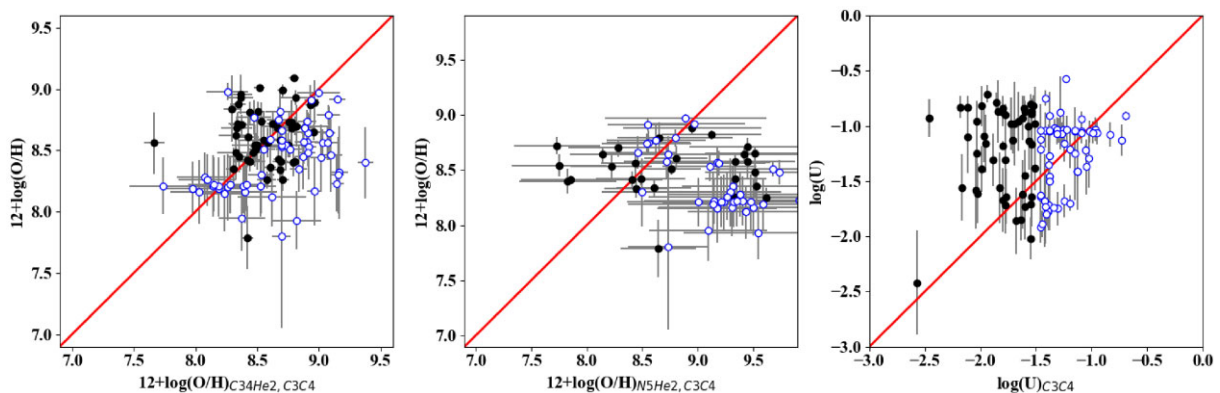


Figure 10. Comparison between the resulting values from HCM-UV, in the vertical axis, and those from different calibrations of Dors et al. (2019), in the respective horizontal axis, as applied to our galaxy sample. In all panels, filled symbols represent objects with assumed dust, while empty symbols represent objects without dust. In the left-hand panel, the C34He2 and C3C4 parameter calibrations are used for O/H; in the middle panel, the N5He2 and C3C4 parameters are used for O/H; and in the right-hand panel, the C3C4 parameter is used for log U . The red solid lines represent the 1:1 relationship in all panels.

Pérez-Montero et al. (2019) for a subset of galaxies with available information in both spectral regions. This is the case for NGC 1068, which was studied in Nagao et al. (2006). Taking emission lines corrected for optical reddening relative to H β , the code HCM predicts $12 + \log(\text{O}/\text{H}) = 8.71$ (8.59), assuming a value $\alpha_{\text{OX}} = -0.8$ (−1.2), which is very close to the value $12 + \log(\text{O}/\text{H}) = 8.68$ (8.57) obtained by HCM-UV using UV emission lines. For the other two galaxies in the sample, Mrk 3 and Mrk 573, also studied in Nagao et al. (2006), optical spectra are available, but no UV O III] is reported at λ 1665 Å preventing a meaningful C/O estimate. Nevertheless, for these two galaxies, a solar N/O ratio was derived from the optical data, allowing us to assume a solar carbon-to-nitrogen ratio to compare the results from the optical and UV spectra. In the case of Mrk 3, we derived $12 + \log(\text{O}/\text{H}) = 8.58$ (8.35) from HCM-UV when we

consider a α_{OX} of -0.8 (−1.2), which is significantly lower than the values derived from the optical lines with HCM, with $12 + \log(\text{O}/\text{H}) = 8.72$ (8.59). For MRK 573, the differences are even larger, with $12 + \log(\text{O}/\text{H}) = 8.49$ (8.26) from the UV and 8.79 (8.68) from the optical.

These differences are unlikely to be significant given (i) the small number of objects for which simultaneous derivation of abundances in both the optical and UV can be performed, (ii) the fact that the associated errors are of the same order of magnitude as these differences, (iii) the strong dependence of the results on the extinction correction, especially in the UV, and (iv) the assumption of a fixed C/N abundance ratio, which is not necessarily well justified. However, it is worth noting that the results are consistent overall and can be used as a reference for our sample of high-redshift galaxies.

5 SUMMARY AND CONCLUSIONS

In this work, we describe and implement the adaptation of the code HCM-UV to the NLR of AGNs to derive oxygen abundances, the chemical carbon–oxygen abundance ratio, and ionization parameters using UV emission line intensities.

According to our analysis based on photoionization models covering different input features, the C3O3 emission line ratio turns out to be a robust indicator of C/O in AGNs, as it depends only to a very small extent on O/H, U , the shape of the considered SED, and the presence of dust grains mixed with the gas, which is of great importance in this spectral region. The determination of C/O is not only important for the correct chemical interpretation of these objects, but also implies a much more accurate determination of metallicity based on the carbon UV emission lines. This result is consistent with what has already been observed for SF objects in Pérez-Montero & Amorín (2017).

On the other hand, the determination of O/H and U , although much more reliable when a previous determination of C/O is provided using the C3O3 parameter, is much more dependent on the assumed input conditions of the models, being particularly sensitive to the assumption of the presence or absence of dust grains mixed with gas. Only models without dust grains are able to reproduce the very low C3C4 values observed in many objects, but the adoption of alternative matter-bounded geometry assumptions should also be explored.

We applied our method to a wide range of data from the literature at different redshifts and we found a large scatter in the O/H and $\log U$ distributions, but with a slightly subsolar mean and, as expected, high excitation. The derivation of C/O was only possible for a small subsample, mainly for quasars with values higher than expected for their derived metallicities, but with a large uncertainty because the emission line of O III] was inaccurately measured at λ 1665 Å. We verified that the prior determination of C/O for this subset dramatically affects the final derivation of their overall metallicity.

Finally, we compared our results with other methods based on the same compiled emission lines, such as the Dors et al. (2019) calibrations, and obtained very consistent results for the C34He2 parameter for O/H and C3C4 for $\log U$, but not such good agreement for N5He2 for O/H. In this case, according to our models, the N V] emission line at λ 1239 Å should only be used in combination with the other lines, since it only provides an estimate of the very highly excited gas phase.

ACKNOWLEDGEMENTS

This work has been partly funded by projects Estallidos7 PID2019-107408GB-C44 (Spanish Ministerio de Ciencia e Innovación), and the Junta de Andalucía for grant EXC/2011 FQM-7058. This work has been also supported by the State Agency for Research of the Spanish MCIU ‘Centro de Excelencia Severo Ochoa’ Program under grant SEV-2017-0709. EPM also acknowledges the assistance from his guide dog Rocko without whose daily help this work would have been much more difficult. RA acknowledges financial support from ANID Fondecyt Regular 1202007. RGB acknowledges financial support from grant PID2019-109067-GB100.

DATA AVAILABILITY

The data underlying this article are available in the article and in its online supplementary material. Alternatively, full Tables 2

and 3 are available at the CDS via <http://cdsarc.u-strasbg.fr/viz-bin/cat/J/MNRAS/Vol/Page>.

REFERENCES

- Allington-Smith J. R., Spinrad H., Djorgovski S., Liebert J., 1988, *MNRAS*, 234, 1091
- Amorín R. et al., 2017, *Nat. Astron.*, 1, 0052
- Asplund M., Grevesse N., Sauval A. J., Scott P., 2009, *ARA&A*, 47, 481
- Berg D. A. et al., 2022, *ApJS*, 261, 31
- Bergeron J., Maccacaro T., Perola C., 1981, *A&A*, 97, 94
- Best P. N., Röttgering H. J. A., Lehnert M. D., 1999, *MNRAS*, 310, 223
- Best P. N., Röttgering H. J. A., Longair M. S., 2000, *MNRAS*, 311, 1
- Bornancini C. G., De Breuck C., de Vries W., Croft S., van Breugel W., Röttgering H., Minniti D., 2007, *MNRAS*, 378, 551
- Byler N., Dalcanton J. J., Conroy C., Johnson B. D., Levesque E. M., Berg D. A., 2018, *ApJ*, 863, 14
- Byler N., Kewley L. J., Rigby J. R., Acharyya A., Berg D. A., Bayliss M., Sharon K., 2020, *ApJ*, 893, 1
- Cardelli J. A., Clayton G. C., Mathis J. S., 1989, *ApJ*, 345, 245
- Castro C. S., Dors O. L., Cardaci M. V., Hägele G. F., 2017, *MNRAS*, 467, 1507
- Chevallard J. et al., 2019, *MNRAS*, 483, 2621
- Cimatti A., di Serego Alighieri S., Vernet J., Cohen M. H., Fosbury R. A. E., 1998, *ApJ*, 499, L21
- Davidson K., 1972, *ApJ*, 171, 213
- Davidson K., 1977, *ApJ*, 218, 20
- De Breuck C., Röttgering H., Miley G., van Breugel W., Best P., 2000, *A&A*, 362, 519
- De Breuck C. et al., 2001, *AJ*, 121, 1241
- De Robertis M. M., Hutchings J. B., Pitts R. E., 1988, *AJ*, 95, 1371
- Dietrich M., Wilhelm-Erkens U., 2000, *A&A*, 354, 17
- Dopita M. A. et al., 2006, *ApJS*, 167, 177
- Dors Jr. O. L., Arellano-Córdova K. Z., Cardaci M. V., Hägele G. F., 2017, *MNRAS*, 468, L113
- Dors O. L., Cardaci M. V., Hägele G. F., Krabbe A. C., 2014, *MNRAS*, 443, 1291
- Dors O. L., Cardaci M. V., Hägele G. F., Rodrigues I., Grebel E. K., Pilyugin L. S., Freitas-Lemes P., Krabbe A. C., 2015, *MNRAS*, 453, 4102
- Dors O. L., Monteiro A. F., Cardaci M. V., Hägele G. F., Krabbe A. C., 2019, *MNRAS*, 486, 5853
- Dors O. L. et al., 2020, *MNRAS*, 492, 468
- Dors O. L., Contini M., Riffel R. A., Pérez-Montero E., Krabbe A. C., Cardaci M. V., Hägele G. F., 2021, *MNRAS*, 501, 1370
- Edmunds M. G., 1990, *MNRAS*, 246, 678
- Feltre A., Charlot S., Gutkin J., 2016a, *MNRAS*, 456, 3354
- Feltre A., Charlot S., Gutkin J., 2016b, *MNRAS*, 456, 3354
- Feltre A. et al., 2020, *A&A*, 641, A118
- Ferland G. J., Baldwin J. A., Korista K. T., Hamann F., Carswell R. F., Phillips M., Wilkes B., Williams R. E., 1996, *ApJ*, 461, 683
- Ferland G. J. et al., 2017, *RMxAA*, 53, 385
- Fernández-Ontiveros J. A., Pérez-Montero E., Vílchez J. M., Amorín R., Spinoglio L., 2021, *A&A*, 652, A23
- Gaskell C. M., Shields G. A., Wampler E. J., 1981, *ApJ*, 249, 443
- Gopal-Krishna, Giraud E., Melnick J., della Valle M., 1995, *A&A*, 303, 705
- Gutkin J., Charlot S., Bruzual G., 2016, *MNRAS*, 462, 1757
- Hamann F., Ferland G., 1992, *ApJ*, 391, L53
- Hamann F., Ferland G., 1993, *ApJ*, 418, 11
- Hamann F., Korista K. T., Ferland G. J., Warner C., Baldwin J., 2002, *ApJ*, 564, 592
- Henry R. B. C., Edmunds M. G., Köppen J., 2000, *ApJ*, 541, 660
- Hirschmann M., Charlot S., Feltre A., Naab T., Somerville R. S., Choi E., 2019, *MNRAS*, 487, 333
- Kewley L. J., Nicholls D. C., Sutherland R. S., 2019, *ARA&A*, 57, 511
- Kinney A. L., Bohlin R. C., Calzetti D., Panagia N., Wyse R. F. G., 1993, *ApJS*, 86, 5
- Köppen J., Hensler G., 2005, *A&A*, 434, 531

- Kraemer S. B., Wu C.-C., Crenshaw D. M., Harrington J. P., 1994a, *ApJ*, 435, 171
- Kraemer S. B., Wu C.-C., Crenshaw D. M., Harrington J. P., 1994b, *ApJ*, 435, 171
- Kurk J. et al., 2013, *A&A*, 549, A63
- Lacy M. et al., 1994, *MNRAS*, 271, 504
- Lacy M., Rawlings S., Hill G. J., Bunker A. J., Ridgway S. E., Stern D., 1999, *MNRAS*, 308, 1096
- Le Fèvre O. et al., 2015, *A&A*, 576, A79
- Le Fèvre O. et al., 2019, *A&A*, 625, A51
- Lilly S. J., 1988, *ApJ*, 333, 161
- Lilly S. J. et al., 2007a, *ApJS*, 172, 70
- Lilly S. J. et al., 2007b, *ApJS*, 172, 70
- Lin Y.-H., Scarlata C., Hayes M., Feltre A., Charlot S., Bongiorno A., Väisänen P., Mogotsi M., 2022, *MNRAS*, 509, 489
- Llerena M. et al., 2022, *A&A*, 659, A16
- Maiolino R., Mannucci F., 2019, *A&AR*, 27, 3
- Malkan M. A., Oke J. B., 1983, *ApJ*, 265, 92
- Maseda M. V. et al., 2017, *A&A*, 608, A4
- Matsuoka K., Nagao T., Maiolino R., Marconi A., Taniguchi Y., 2009, *A&A*, 503, 721
- Matsuoka K., Nagao T., Marconi A., Maiolino R., Mannucci F., Cresci G., Terao K., Ikeda H., 2018, *A&A*, 616, L4
- McCarthy P. J., 1991, *AJ*, 102, 518
- McCarthy P. J., Kapahi V. K., van Breugel W., Subrahmanya C. R., 1990a, *AJ*, 100, 1014
- McCarthy P. J., Spinrad H., van Breugel W., Liebert J., Dickinson M., Djorgovski S., Eisenhardt P., 1990b, *ApJ*, 365, 487
- McCarthy P. J., van Breugel W., Kapahi V. K., Subrahmanya C. R., 1991, *AJ*, 102, 522
- McLure R. J. et al., 2018, *MNRAS*, 479, 25
- Mignoli M. et al., 2019, *A&A*, 626, A9
- Miller B. P., Brandt W. N., Schneider D. P., Gibson R. R., Steffen A. T., Wu J., 2011, *ApJ*, 726, 20
- Mollá M., Vílchez J. M., Gavilán M., Díaz A. I., 2006, *MNRAS*, 372, 1069
- Nagao T., Maiolino R., Marconi A., 2006, *A&A*, 447, 863
- Nakajima K., Fletcher T., Ellis R. S., Robertson B. E., Iwata I., 2018a, *MNRAS*, 477, 2098
- Nakajima K. et al., 2018b, *A&A*, 612, A94
- Onoue M. et al., 2021, *ApJ*, 919, 61
- Osmer P. S., 1980, *ApJ*, 237, 666
- Patrício V. et al., 2016, *MNRAS*, 456, 4191
- Pérez-Díaz B., Pérez-Montero E., Fernández-Ontiveros J. A., Vílchez J. M., 2022, *A&A*, 666, A115
- Pérez-Montero E., 2014, *MNRAS*, 441, 2663
- Pérez-Montero E., Amorín R., 2017, *MNRAS*, 467, 1287
- Pérez-Montero E., Contini T., 2009, *MNRAS*, 398, 949
- Pérez-Montero E., Dors O. L., Vílchez J. M., García-Benito R., Cardaci M. V., Hägele G. F., 2019, *MNRAS*, 489, 2652
- Rawlings S., Lacy M., Blundell K. M., Eales S. A., Bunker A. J., Garrington S. T., 1996, *Nature*, 383, 502
- Rigby J. R. et al., 2018, *AJ*, 155, 104
- Rigby J. R. et al., 2021, *ApJ*, 908, 154
- Roettgering H. J. A., van Ojik R., Miley G. K., Chambers K. C., van Breugel W. J. M., de Koff S., 1997, *A&A*, 326, 505
- Saxena A. et al., 2020, *A&A*, 636, A47
- Saxena A. et al., 2022, *MNRAS*, 517, 1098
- Schaerer D. et al., 2022, *A&A*, 658, L11
- Schmidt K. B. et al., 2021, *A&A*, 654, A80
- Shapley A. E., Steidel C. C., Pettini M., Adelberger K. L., 2003, *ApJ*, 588, 65
- Shapley A. E. et al., 2015, *ApJ*, 801, 88
- Shin J., Woo J.-H., Nagao T., Kim S. C., 2013, *ApJ*, 763, 58
- Simpson C. et al., 1999, *ApJ*, 525, 659
- Snijders M. A. J., Netzer H., Boksenberg A., 1986, *MNRAS*, 222, 549
- Spinrad H., Dey A., Graham J. R., 1995, *ApJ*, 438, L51
- Steidel C. C., Adelberger K. L., Shapley A. E., Pettini M., Dickinson M., Giavalisco M., 2003, *ApJ*, 592, 728
- Steidel C. C. et al., 2014, *ApJ*, 795, 165
- Stern D., Dey A., Spinrad H., Maxfield L., Dickinson M., Schlegel D., González R. A., 1999, *AJ*, 117, 1122
- Stern D. et al., 2002, *ApJ*, 568, 71
- Storchi-Bergmann T., Schmitt H. R., Calzetti D., Kinney A. L., 1998, *AJ*, 115, 909
- Szokoly G. P. et al., 2004, *ApJS*, 155, 271
- Tang M., Stark D. P., Ellis R. S., Charlot S., Feltre A., Shapley A. E., Endsley R., 2022, *MNRAS*, 509, 3102
- Thomas A. D., Kewley L. J., Dopita M. A., Groves B. A., Hopkins A. M., Sutherland R. S., 2019, *ApJ*, 874, 100
- Thuan T. X., 1984, *ApJ*, 281, 126
- Uomoto A., 1984, *ApJ*, 284, 497
- Vanzella E. et al., 2016, *ApJ*, 825, 41
- Villar Martín M., Perna M., Humphrey A., Castro Rodríguez N., Binette L., Pérez González P. G., Mateos S., Cabrera Lavers A., 2020, *A&A*, 634, A116
- Villar-Martín M., Fosbury R. A. E., Binette L., Tadhunter C. N., Rocca-Volmerange B., 1999, *A&A*, 351, 47
- Waddington I., Windhorst R. A., Cohen S. H., Partridge R. B., Spinrad H., Stern D., 1999, *ApJ*, 526, L77
- Yang C., Wang T., Ferland G. J., Dou L., Zhou H., Jiang N., Sheng Z., 2017, *ApJ*, 846, 150

SUPPORTING INFORMATION

Supplementary data are available at *MNRAS* online.

Table 2. List of UV fluxes for our sample of AGN.

Table 3. Chemical abundances estimated from HCM-UV, using the grid of AGN models for $\alpha_{OX} = -1.2$ and the stopping criteria of 98% of free electrons.

Please note: Oxford University Press is not responsible for the content or functionality of any supporting materials supplied by the authors. Any queries (other than missing material) should be directed to the corresponding author for the article.

This paper has been typeset from a $\text{\TeX}/\text{\LaTeX}$ file prepared by the author.